Dalton Transactions

Accepted Manuscript

ROYAL SOCIETY OF CHEMISTRY

www.rsc.org/dalton

Dalton Transactions

Dynamic Article Links ►

Cite this: DOI: 10.1039/c0xx00000x

www.rsc.org/dalton

ARTICLE TYPE

Facile synthesis of g-C_3N_4/$(BiO)_2CO_3$ organic-inorganic 2D nanocomposites as efficient visible light photocatalyst

Wendong Zhang[a], Yanjuan Sun[b], Fan Dong[b*], Wei Zhang[c,*], Shuo Duan[d], Qin Zhang[a]

Received (in XXX, XXX) Xth XXXXXXXXX 20XX, Accepted Xth XXXXXXXXX 20XX

DOI: 10.1039/b000000x

Abstract: Novel g-C_3N_4/$(BiO)_2CO_3$ organic-inorganic nanojunctioned photocatalysts were synthesized by *in situ* depositing $(BiO)_2CO_3$ nanoflakes onto the surface of g-C_3N_4 nanosheets through a one-pot efficient capture of atmospheric CO_2 method at room temperature. The as-synthesized samples were characterized by X-ray diffraction patterns (XRD), Fourier transform infrared (FT-IR), X-ray photoelectron spectroscopy (XPS), transmission electron microscopy (TEM), high-resolution transmission electron microscopy (HRTEM), UV-vis diffuse reflectance spectra (DRS), N_2 adsorption-desorption isotherms and electron spin resonance (ESR). The photocatalytic activity of as-synthesized samples was evaluated by degrading Rhodamine B (RhB) and phenol in aqueous solution under visible-light irradiation. The g-C_3N_4/$(BiO)_2CO_3$ nanojunctions showed much higher visible-light photocatalytic activity than those of pure g-C_3N_4 and $(BiO)_2CO_3$ for the degradation of RhB and phenol. The enhanced photocatalytic activity can be mainly ascribed to the well-matched band structures, dye photosentization and efficient crystal facets coupling interaction between g-C_3N_4 {002} and $(BiO)_2CO_3$ {002}.The $\bullet O_2^-$ radicals were identified as the main active species. Furthermore, the pure $(BiO)_2CO_3$ with highly exposed {002} crystal facet also exhibited the excellent visible-light photoactivity for the degradation of RhB, which can be originated from the indirect dye photosensitization. The present work could provide a new strategy into the efficient utilization of atmospheric CO_2 in green synthetic chemistry.

1. Introduction

Photocatalysis is recognized as an ideal candidate technology, which has been researched for various purposes including environmental remediation, hydrogen evolution, CO_2 fixation, oxygen generation, etc.[1-4] Therefore, considerable efforts have been devoted to developing highly efficient and stable photocatalyst systems over the past decades.[5-7] Nanojunctions-constructed has become one of the most important focus of attention to tune the band gap and improve the photocatalytic performance, due to the synergistic effect between two promising semiconductors.[8-9] The intimately contacted interfaces, well-matched band energies and crystal facets coupling between two semiconductors could efficiently facilitate the separation and transfer of photo-generated electron-hole pairs, results in accelerating the surface photochemical reactions.[10-15] Thus, the development of novel, stable and highly efficient visible light-driven photocatalytic system is still the focus of investigation.

[a] College of Urban Construction and Environmental Engineering, Chongqing University, Chongqing, 400045, China,

[b] Chongqing Key Laboratory of Catalysis and Functional Organic Molecules, Chongqing Technology and Business University, Chongqing, 400067, China,

[c] Key Laboratory of Multi-scale Manufacturing Technology, Chongqing Institute of Green and Intelligent Technology, Chinese Academy of Sciences, 400714, Chongqing, P. R. China,

[d] College of Resource and Environmental Science, Chongqing University, Chongqing, 400045, China,

∗ To whom correspondence should be addressed.

E-mail: dfctbu@126.com (Fan Dong) , zhangwei@cigit.ac.cn (Wei Zhang).

Tel.: +86-23-62769785-605; Fax: +86-23-62769785-605.

Recently, bismuth subcarbonate ($(BiO)_2CO_3$) as novel photocatalysts have triggered great attentions due to their potential applications in fundamental and applied scientific fields.[16-17] However, the pure $(BiO)_2CO_3$ with wide band gap (3.1-3.5 eV) which works only with ultraviolet (<5% fraction of solar light), restricts its practical applications. To date, many efforts have been done to make $(BiO)_2CO_3$ visible light active, such as graphene-decorating (e.g. graphene-wrapping $(BiO)_2CO_3$), [18-19] nonmental-doping (e.g. N-doping $(BiO)_2CO_3$),[20-21] architecture-controlling (e.g. rose-like $(BiO)_2CO_3$ hierarchical microspheres) and nanojunctions-constructing (e.g. $(BiO)_2CO_3$/BiOI, $(BiO)_2CO_3$/$BiVO_4$).[22-25] However, high cost, time consuming and particular reaction conditions restrain their large-scale applications. Thus, it is highly desirable to develop novel and efficient strategies for enhancing the visible light photocatalytic performance of $(BiO)_2CO_3$.

Very recently, graphitic carbon nitride (g-C_3N_4) as a novel organic photocatalyst is attracting increasingly interest owing to its intrinsic physical and chemical properties.[26-27] In particular, some researchers reported that g-C_3N_4 posses typical two dimensional (2D) nanostructure/morphology which could provide a good plane for contact with other semiconductors, resulting the formation of 2D nanojunctions, such as g-C_3N_4/BiOBr,[28-29] g-C_3N_4/rGO,[30] g-C_3N_4/MoS_2,[31] g-C_3N_4/BiOI,[32] g-C_3N_4/Bi_2WO_6,[33] g-C_3N_4/g-C_3N_4,[9] etc. Furthermore, the layered 2D nanojunctions could facilitate the photo-generated charges transfer across the intimate interface, which is expected to improve the photocatalytic performance comparing with individual photocatalyst. However, to the best of our knowledge, little information about the coupling of $(BiO)_2CO_3$ and graphitic carbon nitride (g-C_3N_4) for visible light photocatalysis has been reported.

In the present work, we have designed a novel g-C_3N_4/$(BiO)_2CO_3$ nanojunction photocatalyst by the self-assembly of $(BiO)_2CO_3$ nanoflakes onto the surface of g-C_3N_4 nanosheets through one-pot efficient capture of atmospheric CO_2 at room temperature. Due to the well-matched band energies and coupled crystal facets, the g-C_3N_4/$(BiO)_2CO_3$ nanojunctions showed the significant enhancement in photocatalytic removal of RhB compared with the individual g-C_3N_4 and $(BiO)_2CO_3$. Furthermore, the possible mechanism of excellent visible-light photoactivity in pure $(BiO)_2CO_3$ is proposed. The present work could provide a new strategy to simultaneously manufacture novel photocatalytic materials and efficiently capture atmospheric CO_2 at room temperature.

2. Experimental Section

2.1 Synthesis of g-C_3N_4

All chemicals in this study were analytical grade and used without further treatment. In a typical synthesis, 10 g of thiourea was put into a semi-closed alumina crucible with a cover, and then heated to 550 ^oC at a heating rate of 15 ^oC min^{-1} in a muffle furnace for 2 h in air. After the reaction, the alumina crucible was cooled to room temperature. The resultant g-C_3N_4 were collected and grounded into powders for further use.

2.2 Construction of g-C_3N_4/$(BiO)_2CO_3$ nanojunctions

The preparation process was conducted at room temperature.[34] In a typical synthesis, 2.425g of $Bi(NO_3)_3{\cdot}5H_2O$ was dissolved into 100 mL of aqueous solution containing 4 mL nitric acid and vigorously stirred for 1h (Solution A). Then, 1.275g of g-C_3N_4 was added into the solution A and the mixture was ultrasonicated for 30 min (Suspension B). 15 mL of concentrated $NH_3{\cdot}H_2O$ was added dropwise into the suspension B and pumped air stream at a flow rate of 1.0 L/min for 3 h. The precipitates were collected by filtration, washed thoroughly four times with distilled water and ethanol, and then dried at 60 ^oC overnight to obtain the final products. The pure $(BiO)_2CO_3$ was synthesized under the same conditions without adding g-C_3N_4. The g-C_3N_4, $(BiO)_2CO_3$ and g-C_3N_4/$(BiO)_2CO_3$ nanojunctions were labeled as CN, BOC and CN-BOC, respectively. The schematic illustration of the formation process for 2D g-C_3N_4/$(BiO)_2CO_3$ nanojunctions is presented in Fig. 1.

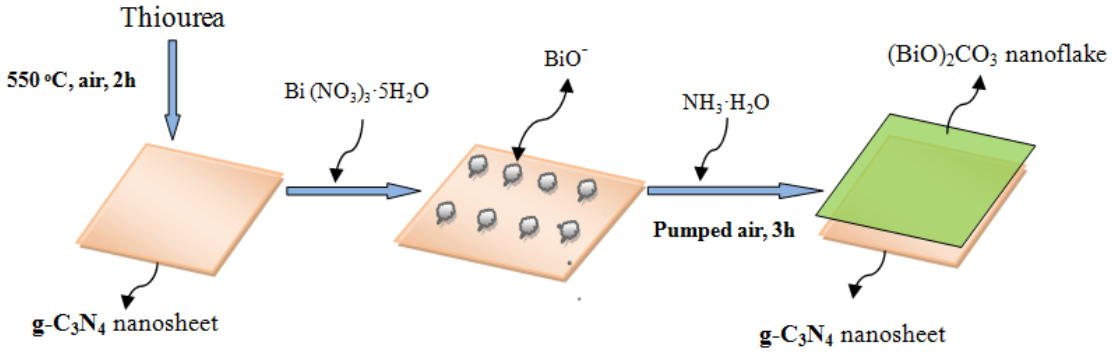

Fig. 1 Schematic illustration of the formation process of two-dimensional (2D) g-C_3N_4/$(BiO)_2CO_3$ nanojunctions.

2.3 Characterization

The crystal phases of the samples were analyzed by X-ray diffraction with Cu Kα radiation (XRD: model D/max

RA, Rigaku Co., Japan). FT-IR spectra were recorded on a Nicolet Nexus spectrometer on samples embedded in KBr pellets. The morphology and structure of the samples were examined by transmission electron microscopy (TEM: JEM-2010, Japan). The UV-vis diffuse reflection spectra were obtained for the dry-pressed disk samples using a Scan UV-vis spectrophotometer (UV-vis DRS: UV-2450, shimadzu, Japan) equipped with an integrating sphere assembly, using $BaSO_4$ as reflectance sample. The spectra were recorded at room temperature in air range from 250 to 800 nm. X-ray photoelectron spectroscopy with Al Kα X-rays (hν = 1486.6 eV) radiation operated at 150 W (XPS: Thermo ESCALAB 250, USA) was used to investigate the surface properties. The shift of the binding energy due to relative surface charging was corrected using the C1s level at 284.8 eV as an internal standard. The nitrogen adsorption–desorption isotherms were determined by the BET method (BET-BJH: ASSP 2020, USA), from which the surface area, pore volume, and average pore diameter were calculated by using the BJH method. All the samples were degassed at 90 ^oC prior to measurements.The electron spin resonance (ESR) signals of •OH and $•O_2^-$ radicals spin-trapped by spin-trap reagent DMPO (5, 5'-dimethyl-1-pirrolin e-N-oxide) in water and methanol were examined on ESR spectrometer (FLsp920, England), respectively. The visible light irradiation source was a 300 W Xe arc lamp (PLS-SXE 300, Beijing) system equipped with a UV cut-off filter (λ = 420 nm).

2.4 Visible light photocatalytic performance

Photocatalytic activity of CN, CN-BOC and BOC for degradation of aqueous Rodamine B (RhB) and phenol was evaluated in a quartz glass reactor. 0.02 g of the as-prepared samples was dispersed in RhB aqueous solution (55 mL, 8 mg/L). The light irradiation system contains a 500 W Xe lamp with a jacket filled with flowing and thermostatted aqueous $NaNO_2$ solution (1 M) between the lamp and the reaction chamber as a filter to block UV light (λ < 400 nm) and eliminate the temperature effect. Before irradiation, the suspension was allowed to reach equilibrium with continuous stirring for 60 min. The degradation efficiency of RhB was evaluated using the UV-vis absorption spectra to measure the peak value of a maximum absorption of RhB solution. During the irradiation, 5mL of suspension was continually collected from the reaction cell at given time intervals for subsequent dye concentration analysis after centrifuging. The RhB solution shows a similar pH value at 6.8, which does not affect the light absorption of RhB. The maximum absorption of RhB is at the wavelength of 552 nm. The maximum absorption of phenol is at the wavelength of 270 nm. The removal ratio η (%) can be calculated as:

$$\eta(\%)=(C_0-C)/C_0\times 100\%$$

Where, C_0 is the initial concentration of RhB considering RhB adsorption on the catalyst and C is the revised concentration after irradiation. The kinetics of photocatalytic RhB removal reaction is a pseudo first order reaction at low RhB concentration as $\ln(C_0/C) = kt$, where k is the apparent reaction rate constant.

3. Results and discussion

3.1 Phase structure. Fig. 2 shows the XRD patterns of the as-synthesized CN, CN-BOC and BOC samples. The two distinct diffraction peaks at 13.2 and 27.6^o in CN correspond to the {100} and {002} crystal facets,[2, 28-29] respectively. All the diffraction peaks for BOC can be highly indexed to pure orthorhombic BOC crystallites (JCPDS–ICDD card No.25-1464). Note that no other diffraction peaks can be detected, indicating that the BOC nanoflakes with high purity have been synthesized by the simple method.[35] These typical diffraction peaks of CN and BOC can also be observed in the nanojunctions, which demonstrate that BOC nanoflakes have been successfully combined with CN nanosheets. It can be found that only the (002) peak in BOC decreases in the nanojunction, indicating that the {002} crystal facet in BOC is highly exposed. Further observation in the XRD pattern clearly shows that the intensity of (100) and (002) peaks in CN decreases when the BOC is introduced. Moreover, the (002) peak of CN also shifted to 28.4^o in the nanojunctions.[29] Besides, the BOC {002} facet covering on CN {002} facet leads to the intensity of (002) peaks in CN and BOC decreasing simultaneously. The results imply that the coupling CN-BOC nanojunctions occur between the BOC {002} facet and CN {002} facet.

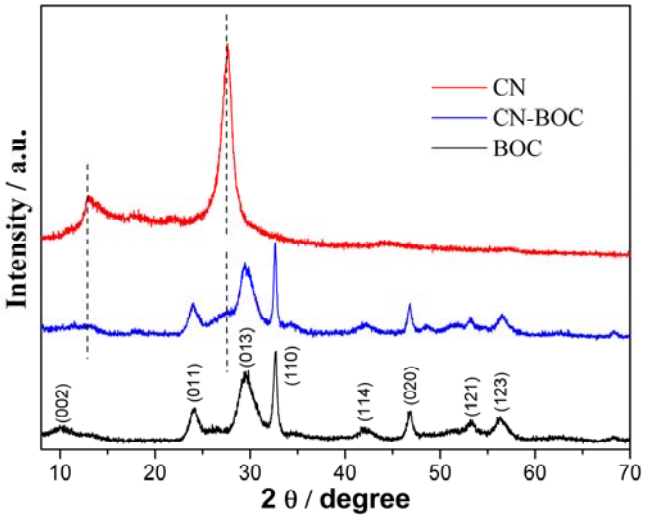

Fig. 2 XRD patterns of the as-synthesized CN, CN-BOC and BOC.

3.2 Chemical composition. Fig. 3 and Fig.S1 show FT-IR spectra for CN, CN-BOC and BOC. For pure CN, the intense band at 810 cm^{-1} is ascribed to the characteristic out of plane bending vibration of s-triazine units, and several intense bands in the 1200-1650 cm^{-1} region represent the typical stretching vibration of the heptazine heterocyclic ring (C_6N_7) units.[36-38] For pure BOC, the characteristic bands at 670 cm^{-1} (in-plane deformation), 820 and 846 cm^{-1} (out-of-plane bending mode), 1067 cm^{-1} (symmetric stretching mode), 1391 and 1468 cm^{-1} (antisymmetric vibration mode) can also be observed.[39] Moreover, the bands in the 3000-3500 cm^{-1} region can be ascribed to the adsorbed H_2O of CN, the characteristic bands at 1640 and 3400-3500 cm^{-1} regions can be to the adsorbed H_2O of BOC. Further observation shows that the typical absorption bands in BOC become weak with the introduction of CN, which implies that the CN-BOC nanojunctions is successfully formed. Furthermore, all typical absorption peaks of pure CN and BOC remain in the CN-BOC nanojunctions, confirming that the CN-BOC nanojunctions are composed of CN and BOC.

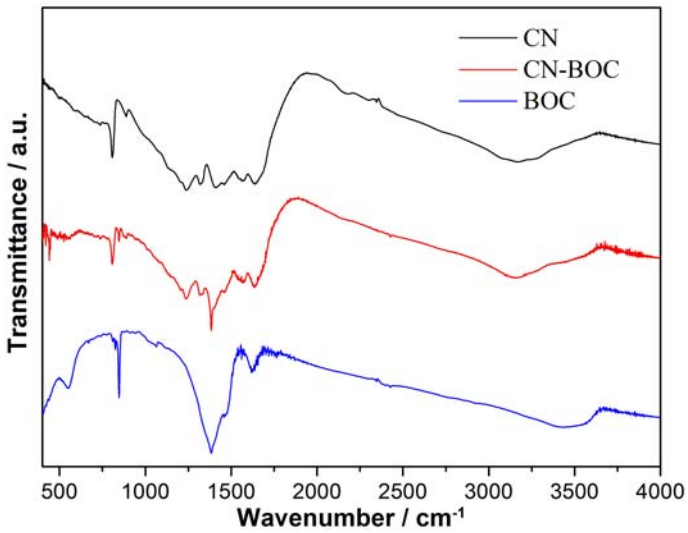

Fig. 3 FT-IR spectra for CN, CN-BOC and BOC.

The XPS measurements were carried out to confirm the coupling mode among atoms in the CN-BOC nanojunctions. Fig. 4a shows two obviously peaks at 159.0 and 164.3 eV, which are indexed to $Bi4f_{7/2}$ and $Bi4f_{5/2}$ in BOC, respectively. Fig. 4b shows the C1s spectra of the CN-BOC. The C peaks at 284.8 and 286.5eV are identified as the typical sp2 C-C bonds of CN and the adventitious carbon species of BOC, respectively. The C peak at 288.5 eV can be assigned to the overlaped peak of the sp2-hybridized carbon in the trizine rings (N-C=N) and the carbonate ion in BOC. Fig. 4c displays the N1s spectra of the CN-BOC. The N peak at 398.1 eV is assigned to sp2 hybridized aromatic N bonded to carbon atoms (C=N-C) and the N peak at 399.8 eV corresponded to the tertiary N bonded to carbon atoms in the form of H-N-(C)2 or N-(C)3. Besides, the N peaks at 404.3 and

406.7 eV are attributed to the π-excitations and the residual nitrate ions in CN-BOC, respectively. Fig. 4d shows the O1s spectra of the CN-BOC. The first O peak at 530.1 eV is characteristic of Bi–O binding energy in BOC. The second and third peaks at 531.4 and 533.1 eV can be indexed to carbonate species and adsorbed H_2O on the materials surface, respectively. Compared with the previously report on pure CN and BOC, no obivious peaks shift can be found in the Bi4f, C1s, N1s and O1s spectra of CN-BOC, suggesting that chemical states of bismuth, carbon, nitrogen and oxygen in CN-BOC are almost the same as the pure CN and BOC.[38-43]

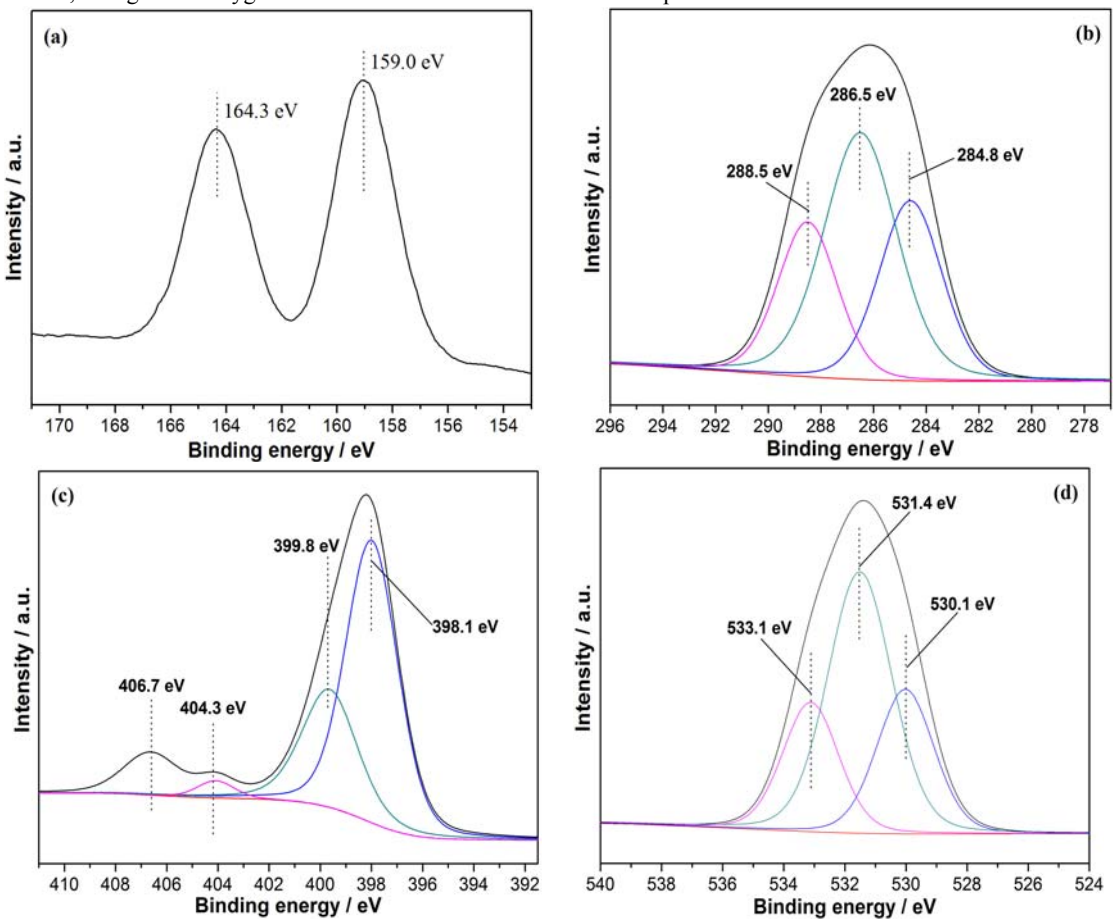

Fig. 4 XPS spectra of the CN-BOC. (a) Bi4f, (b) C1s, (c) N1s and (d) O1s.

3.3 Morphological structure. The low-magnification TEM image (Fig. 5a) shows that individual CN are consisted of smooth and lamellar nanosheets structure with different sizes and irregular shapes. The nanosheets exhibit obviously wrinkles at their edges (Fig. 5b) in order to reduce surface energy due to the interactions with high-energy electrons.[9,44-46] As shown in Fig. 5c, the BOC is composed of large amount of flake-like nanostructures and the size of the nanoflakes is about 30-130 nm. The high-magnification TEM image (Fig. 5d) further confirms that the morphology of BOC is layered aggregation among the nanoflakes. The SAED pattern (inset in Fig. 5d) indicates that single-crystal BOC nanoflakes are with good crystalline and consistent with the XRD result. According to the crystal structure of BOC, the $(BiO)_2^{2+}$ layers and CO_3^{2-} layers are inter-grown with the plane of the CO_3^{2-} group orthogonal to the plane of the $(BiO)_2^{2+}$ layers. Such an inter-grown layered structure would govern the growth of BOC at a certain axis direction to form 2D nanoflake morphology.[20-22] The formation of BOC crystals originates from the chemical reactions between the starting compounds following the Eqs. (1)-(5).[46]

$$Bi(NO_3)_3 + H_2O \rightarrow BiONO_3 + 2H^+ + 2NO_3^- \quad (1)$$

$$NH_3 \cdot H_2O \rightarrow NH_4^+ + OH^- \quad (2)$$

$$BiONO_3 + OH^- \rightarrow BiO(OH) + NO_3^- \quad (3)$$

$$CO_2 + 2OH^- \rightarrow CO_3^{2-} + H_2O \quad (4)$$

$$2BiO(OH) + CO_3^{2-} \rightarrow (BiO)_2CO_3 + 2OH^- \quad (5)$$

Fig. 6a clearly reveals that the BOC nanoflakes are *in situ* self-assembled on the surface of CN nanosheets, the closely contacted interface between CN and BOC results in the formation of 2D nanojunctions. The d-spacing of lattice fringes are measured to be 0.326 and 0.295 nm (Fig. 6b and Fig. S2), corresponding to the {002} crystal facet of CN and {013} crystal facet of BOC, respectively. The fact illustrates that the nanojunctions are successful constructed, which is also well agreement with the XRD result.

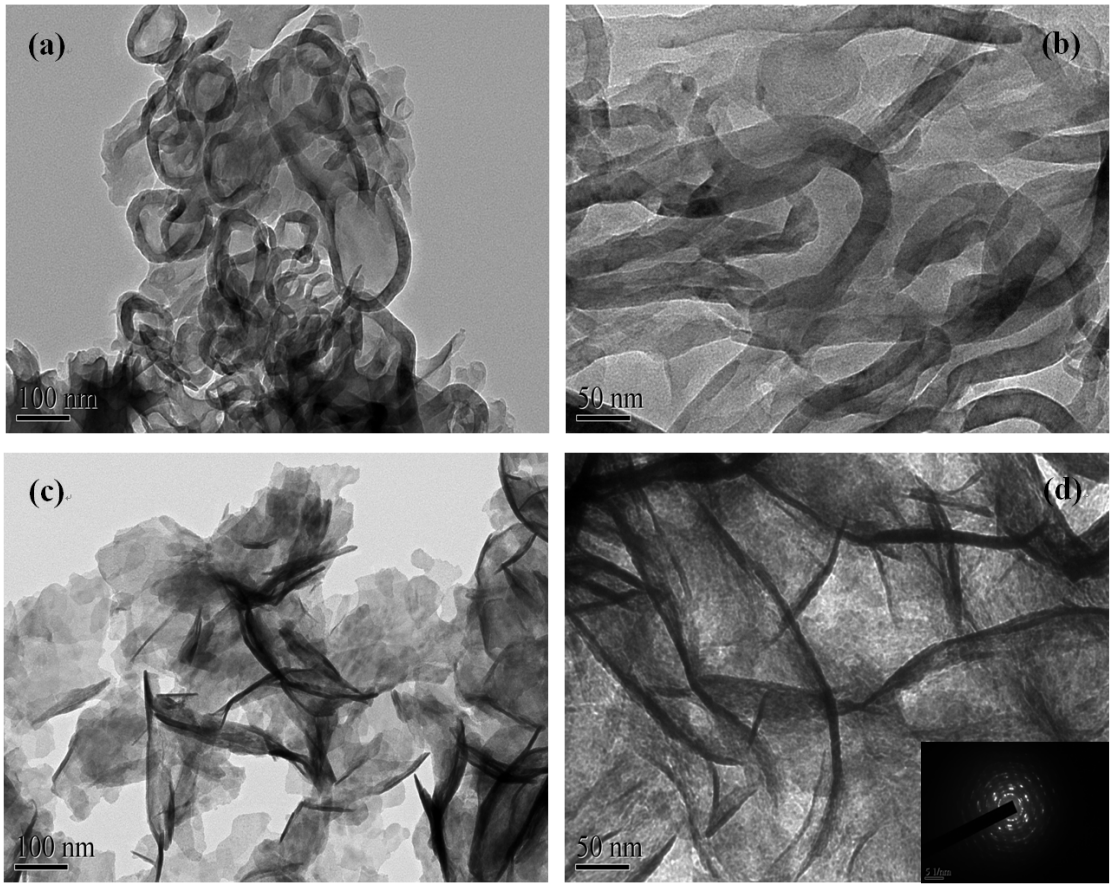

Fig. 5 TEM images of the as-synthesized CN (a, b) and BOC (c, d), SAED pattern of BOC (inset of d).

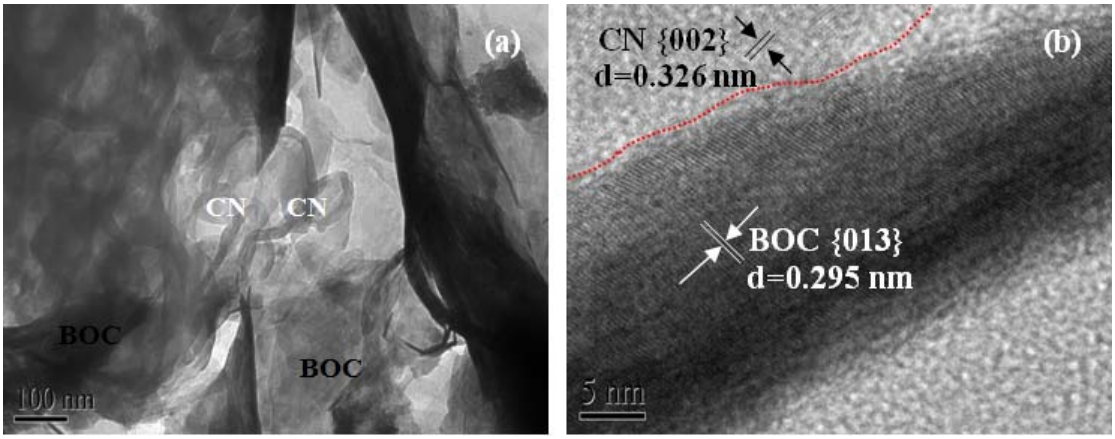

Fig. 6 TEM (a) and HRTEM (b) images of the as-synthesized CN-BOC sample.

3.4 Band gap structure of the nanojuctions. As shown in Fig. 7a, the BOC shows significant light absorption in the UV region. In comparison to BOC, the absorption band edge of CN-BOC exhibits apparently red shift with the introduced of CN, which can be ascribed to the interaction between the CN and BOC semiconductors in the nanojunctions. The band gaps (E_g) of as-synthesized CN and BOC estimated from the intercept of the tangents to the plots of $(\alpha h\nu)^{1/2}$ vs. photo-energy (Fig. 7b) are 2.43 and 3.11 eV, respectively. This fact indicates that the successful construction of 2D CN-BOC nanojunctions could provide great potential in optimizing the band structures and designing novel photocatalysts with desired optical properties.

In order to understand the band structure of CN-BOC nanojunctions, the positions of conduction band (CB) edge and valence band (VB) edge were calculated by a simple theoretical method. The conduction band edge (E_{CB}) of a semiconductor at the point of zero charge (pH_{ZPC}) can be determined by the equation $E_{CB} = X - E_C - 1/2E_g$, where X is the absolute electronegativity of the semiconductor. E_C is the energy of free electrons on the hydrogen scale (~4.5 eV). E_g is the band gap energy of the semiconductor.[46] The calculated CB and VB edge positions of CN

and BOC are listed in the Table 1. A schematic illustration of the band gap structures for the samples is shown in Fig. 8. The band structures of the two components are well-matched with each other. The CN sample can be excited by visible light and generate photo-induced electrons and holes. However, the BOC sample with a wide band gap can only absorb UV light. The relative CB and VB edge positions of CN nanosheets and BOC nanoflakes imply that the well-matched band energies and crystal facets can form heterojunctions at nano level. The photo-generated electrons can transfer from the CB of CN to CB of BOC, which results in efficient separation and transport of photo-induced electrons and holes. Hence, it is expected that the CN-BOC nanojunctions could effectively improve the photocatalytic activity.

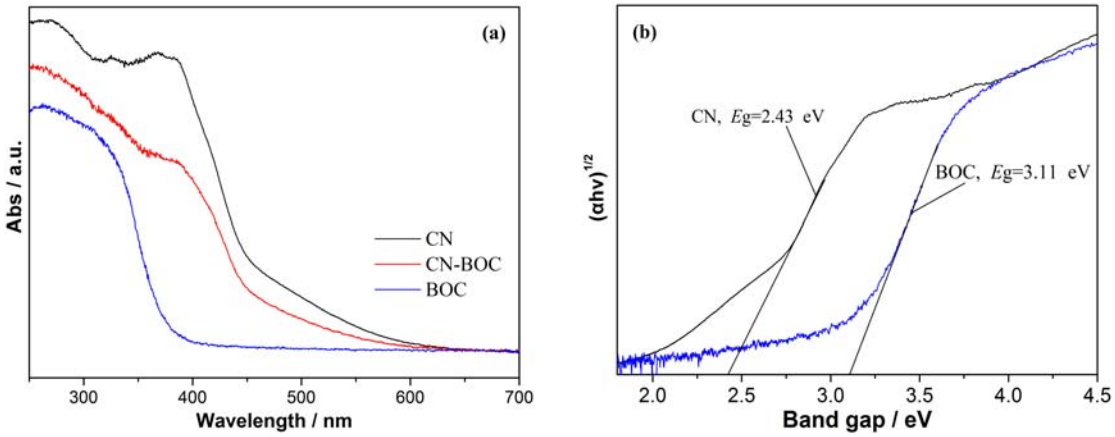

Fig. 7 UV-vis DRS (a) and plots of $(\alpha h\nu)^{1/2}$ vs. photo energy (b) of the as-synthesized CN, CN-BOC and BOC.

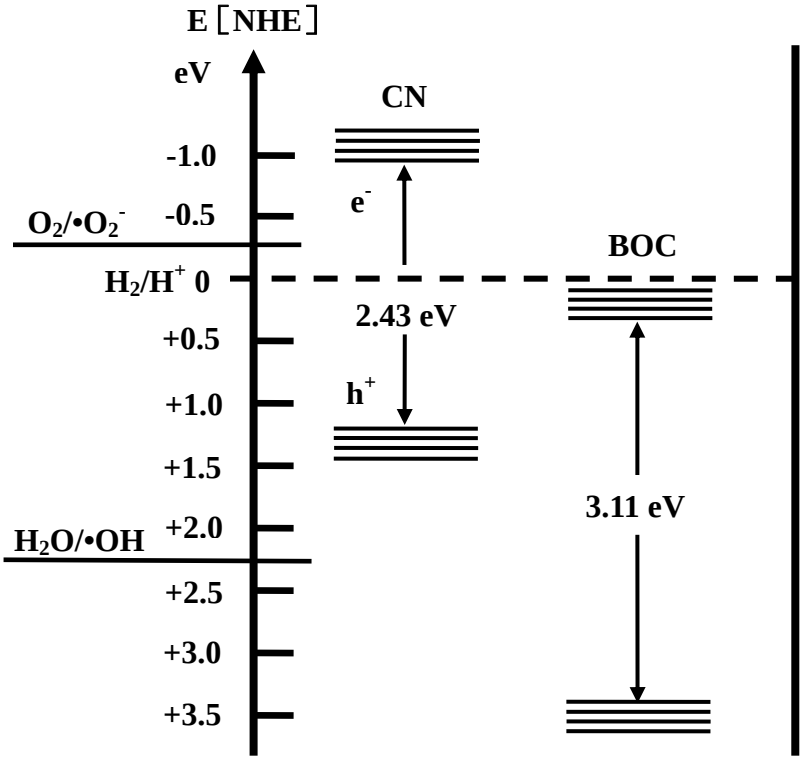

Fig. 8 Schematic illustration of the band gap structures of CN and BOC.

Table 1. Absolute electronegativity, calculated CB edge, calculated VB position and band gap energy for CN and BOC at the point of zero charge.

Semiconductors	Absolute electronegativity (X) (/eV)	Calculated CB position (eV)	Calculated VB position (eV)	Band gap energy E_g (eV)

CN	4.73	-0.99	1.44	2.43
BOC	6.33	0.29	3.37	3.08

Fig. 9 shows the nitrogen adsorption-desorption isotherms and corresponding curves of the pore size distribution for CN, CN-BOC and BOC. The isotherms of CN, CN-BOC and BOC can be classified to type IV (Fig. 9a), which indicates the presence of mesopores. The interconnected porous network could mainly contribute to the formation of mesopores of CN, and the aggregation of nanoflakes could result in the formation of the mesopores of BOC. The specific surface areas are 23, 26 and 15 m^2/g for CN, CN-BOC and BOC (Fig. 9b), respectively. The data illustrates that the aggregation of nanosheets/nanoflakes could play a key role in increasing the special surface during the construction of 2D CN-BOC nanojunctions.

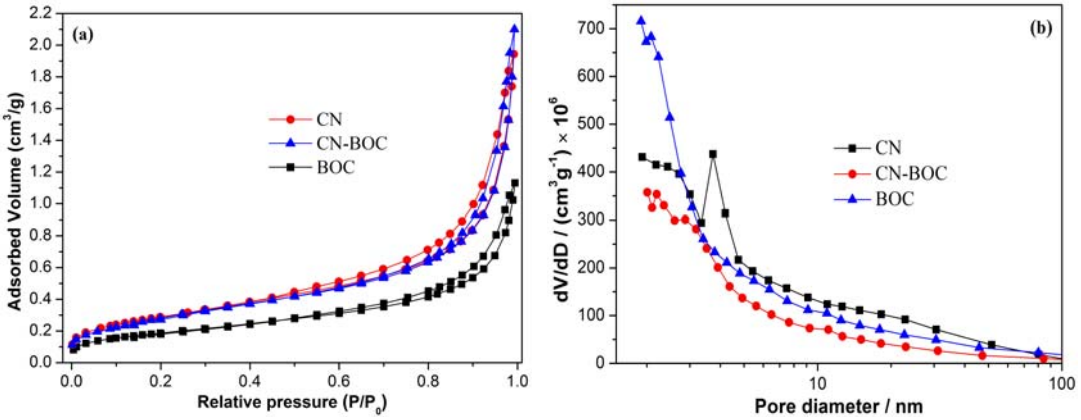

Fig. 9 N_2 adsorption-desorption isotherms (a) and the corresponding pore size distribution curves (b) of CN, CN-BOC and BOC.

3.5 Visible light photocatalytic activitie and mechanism of the activity enhancement. Fig. 10 shows the adsorption and photocatalytic properties of the as-synthesized CN, CN-BOC and BOC samples for removal of aqueous RhB. Fig. 10a displays that no degradation of RhB can be observed in the absence of photocatalyst, indicating that RhB is quite stable and the self-degradation is negligible. It can be seen that the adsorption–desorption equilibrium has reached within 60 min. The adsorption ability is in the following order: CN-BOC (30.9%)> CN (19.5%) > BOC (12.9%), which is well consistent with the S_{BET} result. After 5 h of visible-light irradiation, the individual CN and BOC show relatively low photocatalytic activity compared to CN-BOC nanojunctions. Furthermore, the CN-BOC reveals the highest reaction rate constants (k) of 0.01 min^{-1}, which is almost 2 and 2.5 fold higher than those of the individual CN (0.005 min^{-1}) and BOC (0.004 min^{-1}), respectively.

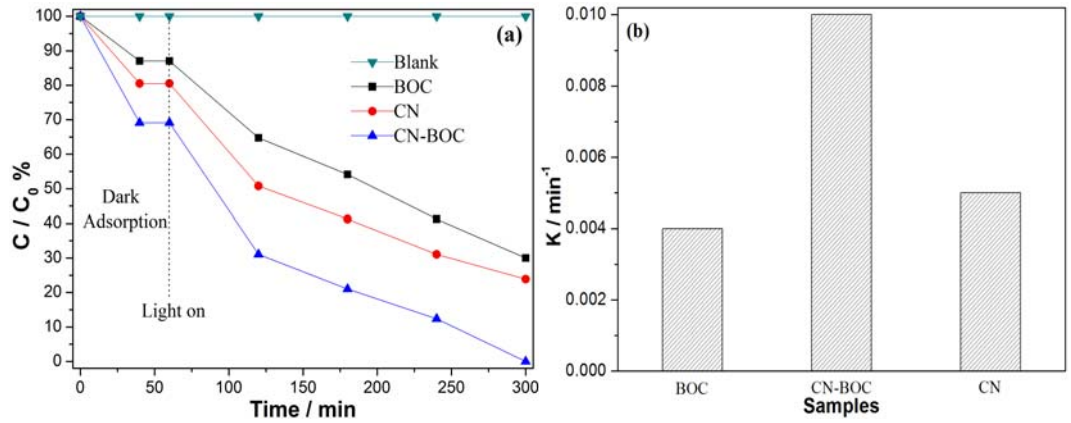

Fig. 10 Adsorption and photocatalytic activity (a) and apparent reaction rate constants (b) of the as-synthesized CN, CN-BOC and BOC for removal of RhB under visible light irradiation (λ > 420 nm).

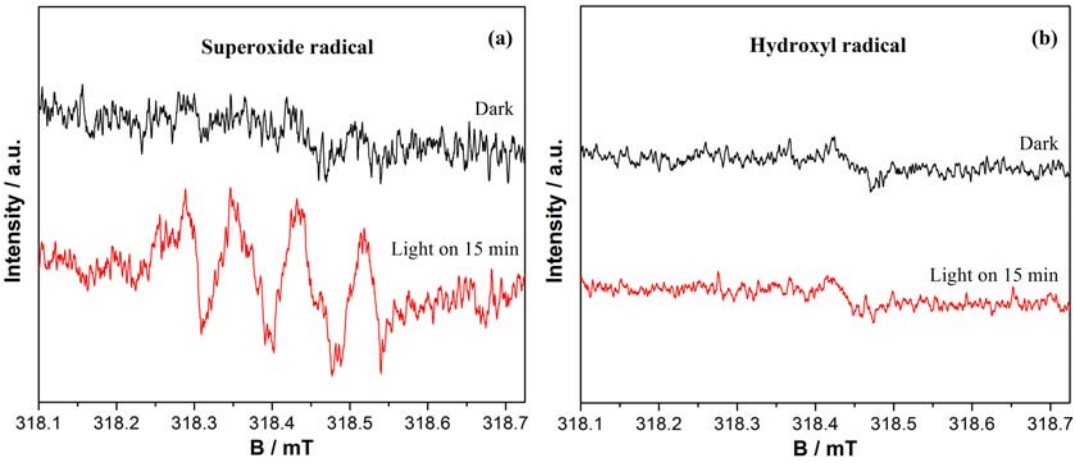

Fig. 11 ESR spectra of radical adduct trapped by DMPO (DMPO-O_2^- and DMPO-•OH) over the CN-BOC nanocomposites without or with the visible light irradiation (λ= 420 ~ 450 nm).

Table 1 shows that the CB of CN (-0.99 eV) is much more negative than the position of O_2/•O_2^- (-0.28 eV vs. NHE). The •O_2^- radicals could be generated by reducing the O_2 with an electron. However, the position of •OH /H_2O (+2.27 eV vs. NHE) is much more positive than the VB of CN (+1.44 eV), therefore, •OH would not be produced by hole oxidizing. The photocatalytic mechanism can be further investigated by electron spin resonance (ESR) technique. DMPO is generally applied to trapping radicals of •OH and •O_2^-. As shown in Fig. 11, •O_2^- radicals could be detected by the ESR under visible light irradiation. However, no •OH radicals can be detected by ESR. This fact demonstrates that •O_2^- radicals are the main active species which play important role during the photo-degradation process.

As we all know, the pure BOC can only work with the UV light due to its wide band gap (3.11 eV). Thus, BOC could not produce photo-generated electron and hole for further photocatalytic degradation of target contaminant under visible-light irradiation (λ > 420 nm). Herein, it is interesting to find that the pure BOC exhibit significantly visible-light photocatalytic activity, which should be attributed to the indirect dye photosensitization process. As shown in Fig.12, the mechanism of indirect dye photosensitization induced degradation on the BOC might proceed in the following procedure.[48-49] First, the RhB molecules are absorbed on the surface of BOC and then transferred into its excited state (RhB*) under visible-light irradiation. Second, the electrons are injected from the RhB* into conduction band of BOC where the electrons are trapped by the molecules oxygen. Third, the electrons in the CB of BOC react with O_2 to produce •O_2^- radicals for further degradation of $RhB^{+\cdot}$, and the BOC is served only as electron-mediator which may be favorable for the effective separation and transfer of the injected electrons and cationic RhB radicals. Thus, the photo-generated electrons in the excited dyes and molecular oxygen play a crucial role in the indirect dye photosensitization process.

After coupling the BOC {002} facet and CN {002} facet, the CN-BOC exhibits remarkable enhancement visible-light photocatalytic activity. After 5h irradiation, the RhB removal ratio of CN, BOC and CN-BOC was 76.1%, 70% and 100%, respectively. The enhancement of photocatalytic activity of CN-BOC nanojunctions could be ascribed to the following factors.[50-55] First, the well-coupled crystal facets, well-matched band structure and layered 2D nanojunctions are favorable for separation and transfer of the photo-induced electrons and holes. Second, the combination of 2D nanosheets increased the surface areas of CN-BOC (26 m^2/g), which is larger than that of pure CN (23 m^2/g) and BOC (15 m^2/g). The larger surface areas could expect to adsorb more reactants and facilitate mass transfer, and provide more activity sites for the photochemical reaction. Third, the indirect dye photosensitization process could also improve the removal probability for the degradation of RhB in the nanojunctions. Furthermore, RhB with E_0= -1.42 V (vs. NHE) demonstrates the highest absorption in the visible region at wavelength of 552 nm. Therefore, both CN and RhB can produce electrons under visible light irradiation. The photo-generated electrons of RhB move into CB of CN quickly, which could make the electrons separation efficient and improve the photocatalytic activity. This research could provide a new perspective for design of 2D nanojunctioned photocatalysts by combining organic-inorganic semiconductors with well-matched band structure and well-coupled crystal facets, and simultaneously develop an effective method to capture and utilization of atmospheric CO_2 in green synthetic chemistry at room temperature.

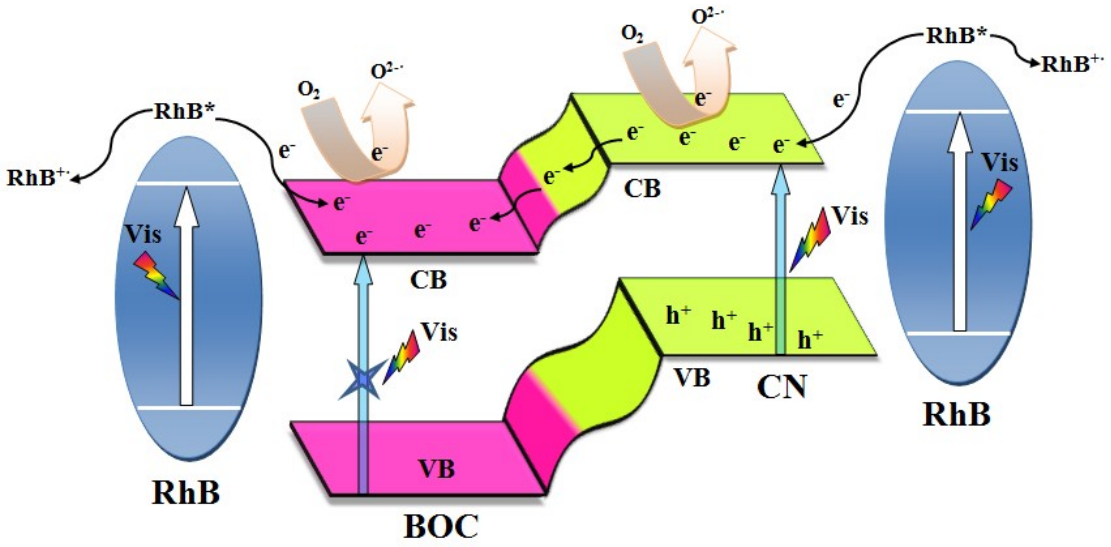

Fig. 12 Mechanism of the photocatalytic degradation of RhB over CN-BOC semiconductor under visible light irradiation (λ > 420 nm).

As shown in Fig.S3, no degradation of phenol can be observed in the absence of photocatalyst, indicating that phenol is quite stable. It can be seen that the adsorption–desorption equilibrium has reached within 60 min. The adsorption ability of CN, CN-BOC and BOC was 6.5%, 4.6% and 9.7%, respectively. After 5h irradiation, the phenol removal ratio of CN and CN-BOC was 13.2% and 19%, respectively. However, no significant photocatalytic degradation of BOC can be detected. The fact illustrates that the photocatalytic activity could be improved by constructed CN-BOC nanojunctions. The enhanced photocatalytic mechanism can be mainly ascribed to the well-matched band structures and efficient crystal facets coupling interaction between g-C_3N_4 {002} and $(BiO)_2CO_3$ {002}.

3.6 Stability of the photocatalyst. The stability of the CN-BOC nanocomposites was investigated for practical application. As shown in Fig. 13, there was only a slight decrease in photocatalytic activity after 4 recycle tests. Furthermore, no significant change can be observed in the XRD patterns (Fig. 14) and TEM images (Fig. 15 and Fig.S4) after 4 repeated photocatalytic runs. The results demonstrate that the as-prepared CN-BOC nanocomposites is relatively stable during the photocatalytic reaction.

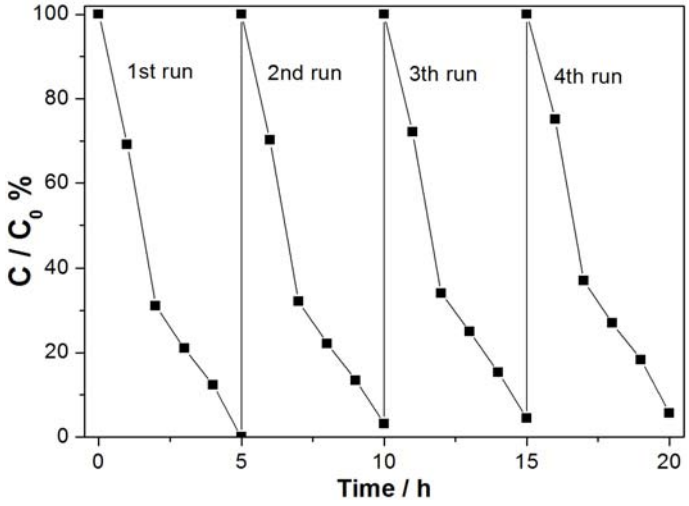

Fig. 13 Recycle run in the photocatalytic degradation of RhB over CN-BOC semiconductor under visible light irradiation (λ > 420 nm).

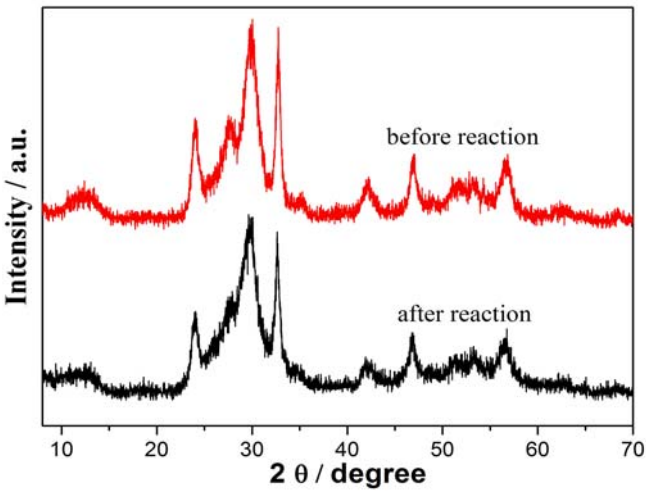

Fig. 14 XRD patterns of CN-BOC before and after 4 recycle runs.

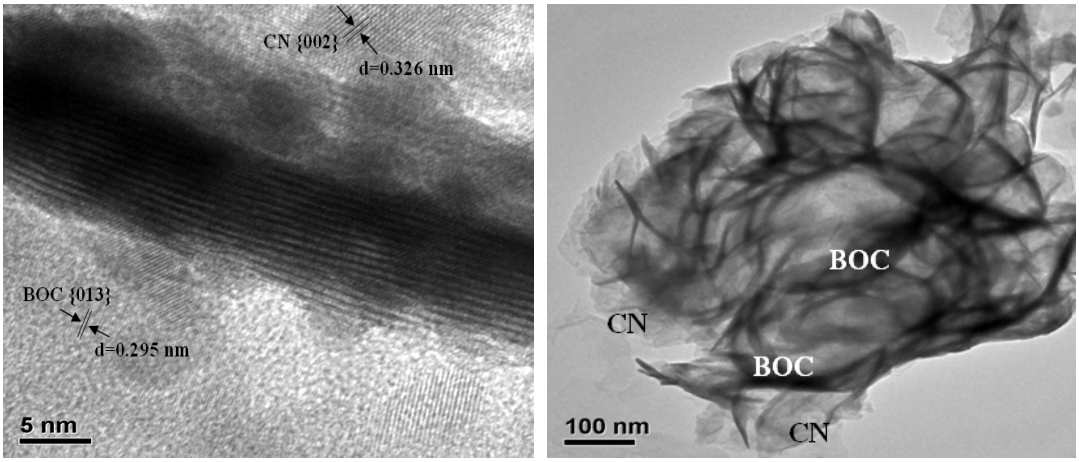

Fig. 15 TEM and HRTEM images of CN-BOC after 4 recycle runs.

4. Conclusion

In summary, CN-BOC nanojunctions were successfully constructed by self-assembly of BOC nanoflakes onto the surface of CN nanosheets by an efficient capture of atmospheric CO_2 method at room temperature. The photocatalytic activity of CN-BOC nanojunctions is significantly enhanced for removal of RhB under visible light irradiation, which can be ascribed to the highly efficient separation and transfer of photo-induced charges at the intimately contacted interface between the BOC {002} facet and C_3N_4 {002} facet with well-matched band structures. Moreover, the dye photosenitization plays important role for improving the photocatalytic activity of CN-BOC nanocomposites during the photocatalytic degradation of RhB. It is also found that the as-synthesized pure BOC show excellent visible-light photocatalytic activity, which is ascribed to the indirect dye photosensitization process of the highly exposed {002} crystal facet. The present work could pave a way for constructing novel 2D visible-light driven nanojunctioned photocatalysts and improving the utilization of atmospheric CO_2 at room temperature.

Acknowledgements

This research is financially supported by the National Natural Science Foundation of China (51108487), the Natural Science Foundation Project of CQ CSTC (cstc2013jcyjA20018), the Science and Technology Project from Chongqing Education Commission (KJ130725).

References

1 X. B. Chen and S. S. Mao. *Chem. Rev*., 2007, **107**, 2891.
2 W. Liu, M. L. Wang, C. X. Xu and S.F. Chen. *Chem. Eng. J*., 2012, **209**, 386.
3 H. Zhou, J. J. Guo, P. Li, T. X. Fan, D. Zhang and J. H. Ye. *Scientific. Reports*., 2013, **1667**, 1.
4 M. A. Rauf and S. S. Ashraf. *Chem. Eng. J*., 2009, **151**, 10.
5 Y. N. Xia, Y. J. Xiong, B. Lim and S. E. Skrabalak. *Angew. Chem. Int. Ed*., 2009, **48**, 60.
6 Y. W. Jun, J. S. Choi and J. Cheon. *Angew. Chem. Int. Ed*., 2006, **45**, 3414.
7 S. W. Liu, J. G. Yu and M. Jaroniec. *Chem. Mater*., 2011, **23**, 4085.
8 Z. Z. Lin and X. C. Wang. *Angew. Chem. Int. Ed*., 2013, **52**, 1.
9 F. Dong, Z. W. Zhao, T. Xiong, Z. L. Ni, W. D. Zhang, Y. J. Sun and W. K. Ho. *ACS Appl. Mater. Interfaces*., 2013, **5**, 11392.
10 J. L. Gunjakar, I. Y. Kim, J. M. Lee, N. S. Lee and S. J. Hwang. *Energy. Environ. Sci*., 2013, **6**, 1008.
11 S. B. Yang, Y. J. Gong, J. S. Zhang, L. Zhan, L. L. Ma, Z. Y. Fang, R. Vajtai, X. C. Wang and P. M. Ajayan. *Adv. Mater*., 2013, **17**, 2452.
12 M. Chhowalla, H. S. Shin, G. Eda, L. J. Li, K. P. Loh and H. Zhang. *Nat. Chem*., 2013, **5**, 263.
13 H. C. Zeng. *J. Mater. Chem*., 2006, 16, 649.
14 X. Huang, Z. Y. Zeng and H. Zhang. *Chem. Soc. Rev*., 2013, **42**, 1934.
15 Q. J. Xiang, J. G. Yu and M. Jaroniec. *Chem. Soc. Rev*., 2012, **41**, 782.
16 Y. Zheng, F. Duan, M. Chen and Y. Xie. *J. Mol. Catal. A: Chem*., 2010, **317**, 34.
17 L. Chen, R. Huang, S. F. Yin, S. L. Luo and C. T. Au. *Chem. Eng. J*., 2012, **193-194**, 123.
18 P. Madhusudan, J. G. Yu, W. G. Wang, B. Cheng and G. Liu. *Dalton. Trans*., 2012, **41**, 14345.
19 Y. L. Zhang, D. Y. Li, Y. G. Zhang, X. F. Zhou, S. J. Guo and L. B. Ya*ng. J. Mater. Chem. A.,* 2014, DOI: 10.1039/C4TA00088A.
20 F. Dong, Y. J. Sun, W. K. Ho and Z. B. Wu. *Dalton. Trans*., 2012, **41**, 8270.
21 F. Dong, Y. J. Sun, M. Fu, W. K. Ho, S. C. Lee and Z. B. Wu. *Langmuir*., 2012, **28**, 766.
22 F. Dong, S. C. Lee, Z. B. Wu, Y. Huang, M. Fu, W. K. Ho, S. C. Zou and B. Wang. *J. Hazard. Mater*., 2011, **195**, 346.
23 T. Zhao, J. Zai, M. Xu, Q. Zou, Y. Su, K. Wang and X. Qian. *CrystEngComm*., 2011, **13**, 4010.
24 L. Chen, S. F. Yin, S. L. Luo, R. Huang, Q. Zhang, T. Hong and P. C. T. Au. *Ind. Eng. Chem. Res*., 2012, **51**, 6760.
25 P. Madhusudan, J. Ran, J. Zhang, J. Yu and G. Liu. *Appl. Catal. B*., 2011, **110**, 286.
26 X. C. Wang, S. Blechert and M. Antonietti. *ACS Catal*., 2012, **2**, 1596.
27 X. G. Ma, Y. H. Lv, J. Xu,Y. F. Liu, R. Q. Zhang and Y. F. Zhu. *J. Phys. Chem. C*., 2012, **116**, 23485.
28 J. Fu, Y. L. Tian, B. B. Chang, F. N. Xi and X. P. Dong. *J. Mater. Chem*., 2012, **22**, 21159.
29 L. Q. Ye, J. Y. Liu, Z. Jiang, T. Y. Peng and L. Zan. *Appl. Catal. B*., 2013, **142–143**, 1.
30 Y. B. Li, H. M. Zhang, P. Liu, D. Wang, Y. Li and H. J. Zhao. *Small*., 2013, **9**, 3336.
31 Y. D. Hou, A. B. Laursen, J. S. Zhang, G. G. Zhang, Y. S. Zhu, X. C. Wang, S. Dahl and I. Chorkendorff. *Angew. Chem. Int. Ed*., 2013, **52**, 1.
32 D. L. Jiang, L. L. Chen, J. J. Zhu, M. Chen, W. D. Shi and J. M. Xie. *Dalton. Trans*., 2013, **42**, 15726.
33 Y. J. Wang, X. J. Bai, C. S. Pan, J. He and Y. F. Zhu. *J. Mater. Chem*., 2012, **22**, 11568.
34 F. Dong, J. Bian, Y. J. Sun, T. Xiong and W. D. Zhang. *CrystEngComm*., 2014, **16**, 3592.
35 F. Dong, H. T. Liu, W. K. Ho, M. Fu and Z. B. Wu. *Chem. Eng. J*., 2013, **214**, 198.
36 J. S. Zhang, J. H. Sun, K. Maeda, K. Domen, P. Liu, M. Antonietti, X. Z. Fu and X. C. Wang. *Energy Environ. Sci*., 2011, **4**, 675.
37 S. C. Yan, Z. S. Li and Z. G. Zou. *Langmuir*., 2009, **25**, 10397.
38 F. Dong, L. W. Wu, Y. J. Sun, M. Fu, Z. B. Wu and S. C. Lee. *J. Mater. Chem.,* 2011, **21**, 15171.
39 F. Dong, A. M. Zheng, Y. J. Sun, M. Fu, B. Q. Jiang, W. K. Ho, S. C. Lee and Z. B. Wu. *CrystEngComm*., 2012, **14**, 3534.
40 R. Chen, M. H. So, J. Yang, F. Deng, C. M. Che and H. Sun. *Chem. Comm*., 2006, **21**, 2265.
41 H. Cheng, B. Huang, K. Yang, Z. Wang, X. Qin, X. Zhang and Y. Dai. *ChemPhysChem*., 2010, **11**, 2167.
42 Y. J. Cui, Z. X. Ding, X. Z. Fu and X. C. Wang. *Angew. Chem. Int. Ed*., 2012, **51**, 11814.
43 G. H. Dong, K. Zhao and L. Z. Zhang. *Chem. Commun*., 2012, **48**, 6178.
44 X. H. Li, X. C. Wang and M. Antonietti. *Chem. Sci*., 2012, **3**, 2170.
45 J. Xu, Y. J. Wang and Y. F. Zhu. *Langmuir*., 2013, **29**, 10566.
46 T. Selvamani, A. M. Asiri, A. O. Al-Youbi and S. Anandan. *Mater. Sci. Forum*., 2013, **764**, 169.
47 W. D. Zhang, Q. Zhang and F. Dong. *Ind. Eng. Chem. Res*., 2013, **52**, 6740.
48 J. Jiang, K. Zhao, X. Y. Xiao and L. Z. Zhang. *J. Am. Chem. Soc*., 2012, **134**, 4473.
49 G. Liu, J. C. Yu, G. Q. Lu and H. M. Cheng. *Chem. Commun*., 2012, **134**, 4473.
50 S. C. Yan, S. B. Lv, Z. S. Li and Z. G. Zou. *Dalton. Trans*., 2010, **39**, 1488.
51 H. W. Kang, S. N. Lim, D. S. Song and S. B. Park. *Int. J. Hydrogen. Energ*., 2012, **37**, 11602.

52 F. Dong, Y. J. Sun, M. Fu, Z. B. Wu and S. C. Lee. *J. Hazard. Mater*., 2012, **219–220**, 26.
53 Z. H. Ai, W. K. Ho, S. C. Lee. *J. Phys. Chem. C*., 2011, **115**, 25330.
54 Y. J. Wang, R. Shi, J. Lin and Y. F. Zhu. *Energy. Environ. Sci*., 2011, **4**, 2922.
55 S. F. Chen, L. Ji, W. M. Tang and X. L. Fu. *Dalton. Trans*., 2013, **42**, 10759.

Table of contents entry

The 2D g-C_3N_4/$(BiO)_2CO_3$ organic-inorganic nanojunctions of were constructed by *in situ* depositing $(BiO)_2CO_3$ nanoflakes on the surface of g-C_3N_4 nanosheets for highly active visible light photocatalysis.